UNIVERSITY OF CALIFORNIA, SAN DIEGO

In-vitro Validation for Kawasaki Disease Hemodynamics

A Thesis submitted in partial satisfaction of the requirements
for the degree Master of Science

in

Engineering Sciences (Mechanical Engineering)

by

Alice Huang

Committee in charge:

Professor Alison Marsden, Chair
Professor Juan C Lasheras
Professor Juan Carlos del Alamo

2010

ProQuest LLC
789 East Eisenhower Parkway
P.O. Box 1346
Ann Arbor, MI 48106-1346

The Thesis of Alice Huang is approved and it is acceptable in quality form for publication on microfilm and electronically:

Chair

University of California, San Diego

2010

Dedication

I want to dedicate this thesis to my parents, Jim and Joann Huang, who have encouraged me to do whatever I wished, including a Master's degree in mechanical engineering, and my friends and peers who encouraged me along research and writing.

Table of Contents

List of Figures

List of Tables

Acknowledgements

I would like to acknowledge Professor Alison Marsden for giving me the opportunity to be involved in this research endeavor, including funding from an NIHR21 Grant and her guidance throughout my graduate schooling.

This thesis would not have been possible without Dr. Juan Lasheras's guidance in experimentation with PIV as well as direction through this project. I am grateful to receive PIV help from Kai Szeto and Tran Nguyen.

I am indebted to my partner, Craig Vermeyen, for teaching me the phantom construction process and assisting in PIV experimentation. My sincere thanks goes to Tom Chalfant, who made the pulsatile input possible through numerous attempts at fixing the UHDC pump.

I would like to acknowledge Dibyendu Sengupta in providing Figure 1.2, Figure 1.2, Figure 3.1, Figure 3.2, the time he contributed toward making the modified 3-D model in Figure 3.3, and the computational simulation results presented throughout Chapter 1.2.

ABSTRACT OF THE THESIS

In-vitro Validation for Kawasaki Disease Hemodynamics

by

Alice Huang

Master of Science in Engineering Sciences (Mechanical Engineering)

University of California, San Diego, 2010

Professor Alison Marsden, Chair

Simulations have been used to study cardiovascular treatment and diseases, but validation of these simulations with in-vitro or in-vivo methods remain a challenge. In creating an experimental set-up to closely match physiological conditions, this in-vitro validation study aims to increase our confidence in simulation methods and results for hemodynamics in aneurysms caused by Kawasaki Disease.

In this project, we construct a three-dimensional, optically-clear flow phantom from a patient specific computer solid model, in which physiologically relevant

boundary conditions are created for PIV measurements. The PIV data is then compared to computational simulation data to demonstrate that the simulation data is able to reproduce similar flow features such as recirculation areas and local velocity profiles.

With these preliminary results from PIV, though not yet sufficient to fully validate the corresponding simulation results, we demonstrate the feasibility of the experimental validation set-up, including model construction and PIV measurements. This establishes a framework for future validation efforts in a range of cardiovascular disease applications using the experimental methods developed in this thesis.

Chapter 1. Background

1.1. Kawasaki Disease

Kawasaki disease (KD) is the leading cause of heart disease in children, with the majority of cases occurring at or less than 5 years of age. The cause of KD currently remains a mystery; it may be an autoimmune disorder affecting mucus membranes, lymph nodes, walls of blood vessels, and the heart (Kawasaki, 1967). There exist no diagnostic tests specifically for KD, therefore delay in treatment is common and can lead to high risk of developing coronary artery aneurysms (Burns & Glode, Kawasaki Syndrome, 2004).

The majority of diagnoses are made based on patients having most of the classic symptoms. KD symptoms include persistent high fever of at least 104°F (39°C) for at least five days. The second phase typically begins within two weeks of fever onset: the skin on hands and feet may begin to peel in large pieces, and the patient may experience joint pain, diarrhea, vomiting, or abdominal pain (Burns & Glode, Kawasaki Syndrome, 2004).

With early detection, full recovery can be expected. Medicine used to treat KD includes intravenous immunoglobulin and aspirin (Suzuki, Miyagawa-Tomita, Komatsu, Nishikawa, Sakomura, & Horie, 1986). Symptoms often disappear within just 2 days of the start of treatment. Heart problems usually do not develop if KD is treated within 10 days of onset of symptoms.

If left untreated, for 25% of the patients, KD has been observed to cause inflammation of blood vessels in the arteries, especially the coronary arteries, as shown in Figure 1.1. One percent of patients die from complications of coronary blood vessel inflammation (Burns, Shike, Gordon, Malhotra, Schoenwetter, & Kawasaki, 1996). This inflammation may lead to aneurysms, which could lead to thrombosis and cause myocardial infarction in the most severe cases.

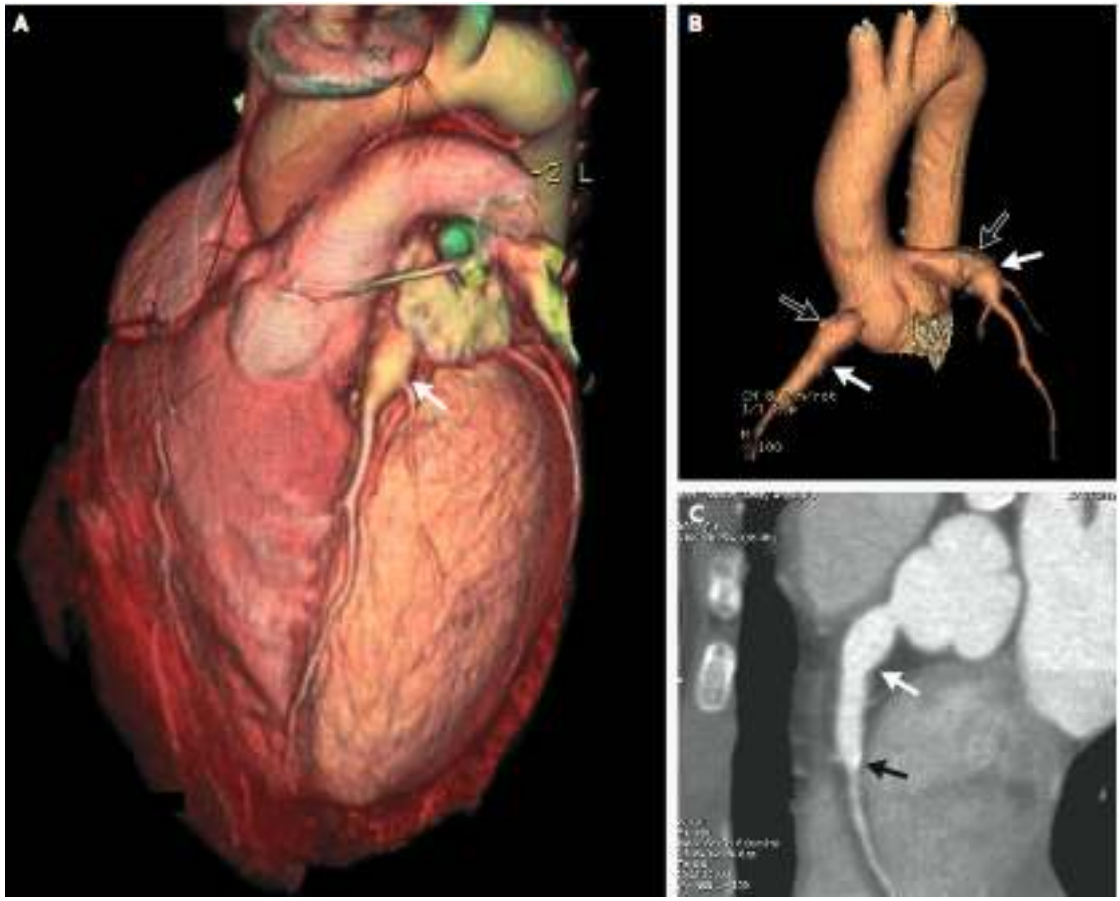

Figure 1.1: Computed Tomography (CT) angiogram from 12-years-old patient

Physicians have to assess the severity of aneurysms and decide which, if any, interventions to pursue and when. Possible interventional strategies include: anticoagulation, angioplasty, stent placement, or coronary artery bypass surgery. There

are no established clinical guidelines for making the best choice, and it is a difficult decision particularly because patients are otherwise healthy. Therefore, there is an unmet clinical need for an aneurysm risk assessment tool to justify intervention decisions.

1.2. Cardiovascular Flow Simulation

Previous work has illustrated an important relationship between hemodynamics and progression of thrombus formation (Strony, Beaudoin, Brands, & Adelman, 1993). In some extreme cases, KD patients have aneurysms comparable in size to the aorta. These aneurysms put patients at risk for ischemia from stenosis and myocardial infarction, and for sudden death or permanent heart damage.

It is currently an open area of research to quantify flow in the coronary arteries due to insufficient resolution in MRI. On the other hand, CT angiography, which has sufficient resolution, is unable to provide fluid flow data. Facing the lack of clinical data, realistic simulations will aid in increasing understanding of aneurysm hemodynamics. Simulation plays a key role in understanding hemodynamics of many cardiovascular diseases and treatments, including bypass grafting (Leuprecht, Perktold, Prosi, Berk, Wolfgang, & Schima, 2002), cardiovascular treatment planning (Wilson, Arko, & Taylor, 2004), atherosclerosis in the carotid artery (Taylor, Hughes, & Zarins, 1998), abdominal aorta (Tang, Cheng, Draney, Wilson, Tsao, & Herfkens, 2006), cerebral-vascular flow (Isaksen, Bazilevs, Kvamsdal, Zhang, Kaspersen, & Waterloo, 2008), congenital heart disease (Marsden, Bernstein, Reddy, Shadden, Spilker, & Chan, 2009), and coronary stents (LaDisa, Guler, Olson, Hettrick, Kersten, & Warltier,

2003). To increase our confidence in simulation results, a physical flow phantom, mimicking in similar setup as shown in Figure 1.2, will be constructed to verify the validity of developed simulation tools.

The goal of the Marsden Research group is to develop a quantitative, computer-based thrombotic risk assessment tool that can be validated in future studies using an established mouse model of KD aneurysm (Duong, Silverman, Bissessar, & Yeung, 2003). This tool is proposed to be used by physicians clinically to differentiate high-risk patients from low-risk patients.

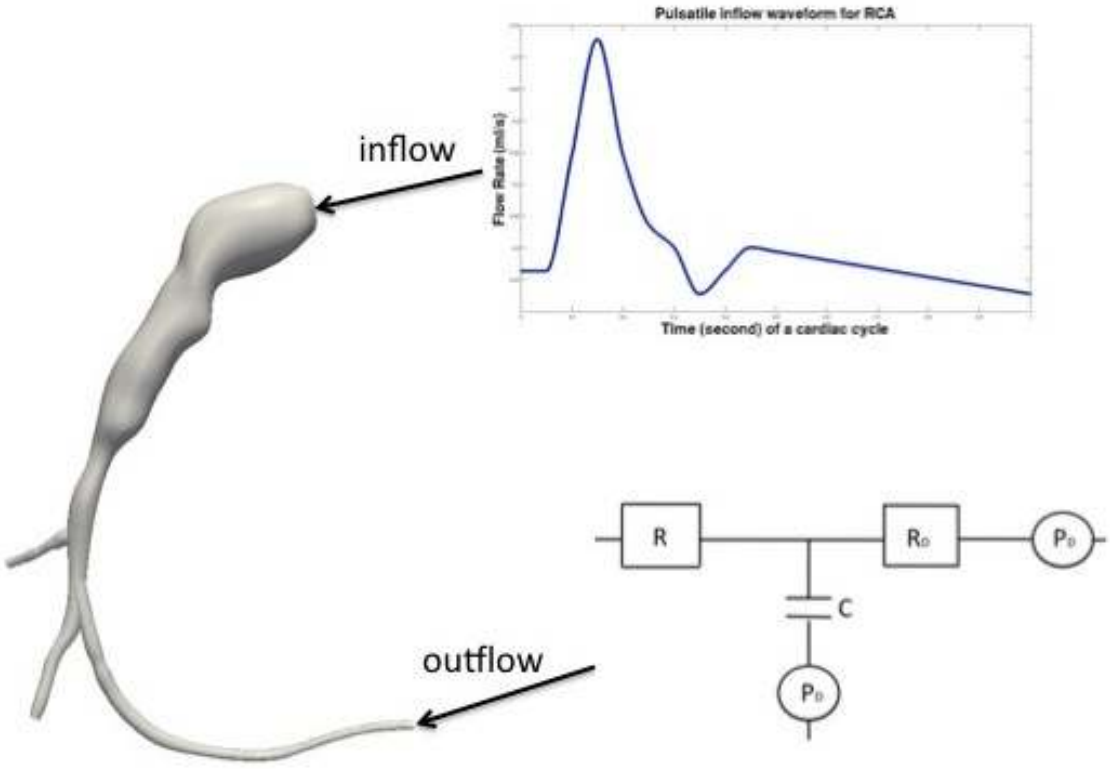

Figure 1.2: RCA inflow waveform and outflow resistance model

1.3. **Phantom construction**

In order to use particle image velocimetry (PIV) to measure the velocity structure, the flow vessel needs to be smooth, clear for imaging, and optically compatible with the laser in use. We can construct the flow path negative using rapid prototyping and path positive by mold casting with soluble material. The product has a block shape with flow path embedded. (Palafox, Wicker, & Elkins, 2003) Compared to traditional casting techniques, this method allows the product to be free of seam lines. To reduce refraction during PIV measurement process, optically-clear material, such as silicone, is commonly used. (Canton, Levy, Lasheras, & Nelson, 2005)

For complex geometries embedded in a block, it is easy to induce refraction through flow curvature, causing inaccuracies in the PIV measurements. To reduce the refraction, a dip-spin coating manufacturing system has been developed by University of Texas to accurately construct thin-walled vessels of complex geometries (Cortez, Quintana, & Wicker, 2007). This method provides consistent thickness as well as accurate geometry for any shape and size of vessels.

Due to this method's long setup time and the simplicity of the geometry in study, the dip-spin process was not replicated in this thesis. However, this method should be explored in future works.

1.4. **Flow similarity**

The right coronary artery (RCA) geometry was scaled up by a factor of 2 for model construction (discussed in Chapter 3.2). In order to enforce flow similarity with physiological conditions, the Reynolds number and the Womersley number should be

preserved (Hale, McDonald, & Womersley, 1955). The Reynolds number quantifies the importance of inertial versus viscous forces for the given flow conditions. The Womersley number quantifies the pulsatile flow frequency in relations to viscous effects.

To compensate for the doubling of model size, the average flow rate, flow frequency, and fluid kinematic viscosity of the phantom are adjusted to match Reynold's and Womersley numbers.

$$\mathrm{Re} = \frac{\bar{V}D}{\upsilon}$$

$$\alpha = R\sqrt{\frac{\omega}{\upsilon}}$$

Using the approximation that the RCA inlet is a circle and $\bar{Q} = \bar{V}A$,

$$\mathrm{Re} = \frac{\bar{Q}D}{A\upsilon} = \frac{4}{\upsilon\pi}\frac{\bar{Q}}{D} = 36$$

$$\alpha = \frac{D}{2}\sqrt{\frac{\omega}{\upsilon}} = \frac{D}{2}\sqrt{\frac{2\pi/T}{\upsilon}}$$

With the doubled diameter D, we also double flow rate to keep Reynolds number at 36. To maintain the same Womersley number, the time period is elongated by four times.

Chapter 2. Experimental Setup

The experimental setup is illustrated in Figure 2.1 schematically. The layout includes the UHDC Pump (Shelley Medical, London, Ontario, Canada), the KD block phantom, and the PIV system (TSI Inc., St. Paul, MN, USA).

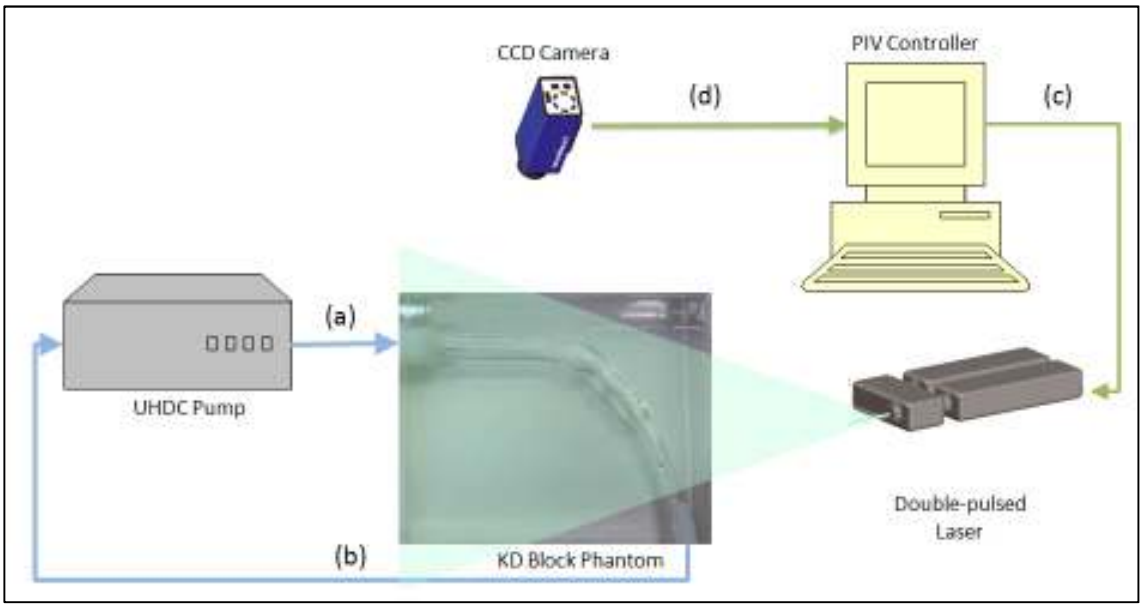

Figure 2.1: Experimental setup diagram

The UHDC pump provides pulsatile fluid flow to simulate physiologically representative flow waveforms. Figure 2.1 (a) and (b) are the fluid in-flow and out-flow from the pump.

The KD block phantom was constructed following the steps as described in Chapter 3.2. The rapid-prototyped geometry was first cast in resin to make a resin mold. Wax models were made from the resin mold, then casted in silicone. Lastly, the wax was melted out of the silicone block.

The PIV system hardware consists of synchronized Yd:YAG laser and CCD camera for illuminating the phantom, shown as (c) in Figure 2.1, and taking image data, shown as (d) in Figure 2.1. The laser and camera are controlled by the software Insight 3G package; Insight 3G also provides pre- and post-processing options for analyzing acquired images

Chapter 3. Phantom Construction Procedure

3.1. Vascular Modeling

Anatomic models were reconstructed from Computed Tomography (CT) loaded into the SimVascular software package, following the method used in published research (Yang, Feinstein, & Marsden, 2010). The steps for model construction are illustrated in Figure 3.1 using LCA (left coronary artery) data:

i. Construct paths through center of vessels
ii. Segmentation of vessels
iii. Loft vessels segments together
iv. Generate mesh

The reconstructed model for the LCA and RCA are shown in Figure 3.2. A simplified version of the RCA was made; simplification includes extending the inlet and outlet, while preserving the aneurysm and stenosis geometry of the RCA.

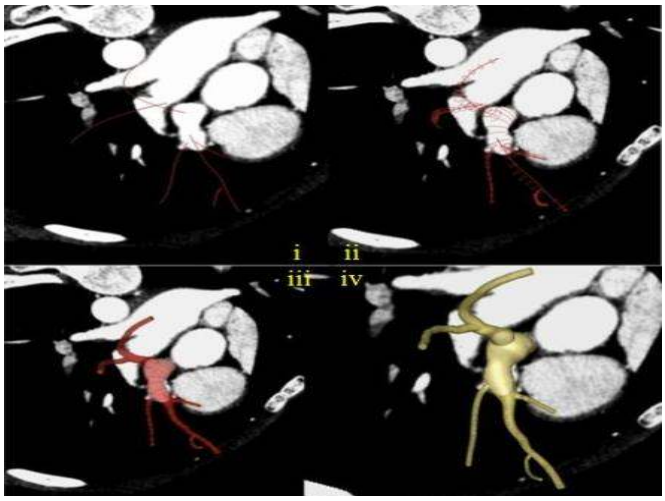

Figure 3.1: Steps to reconstruct 3D model

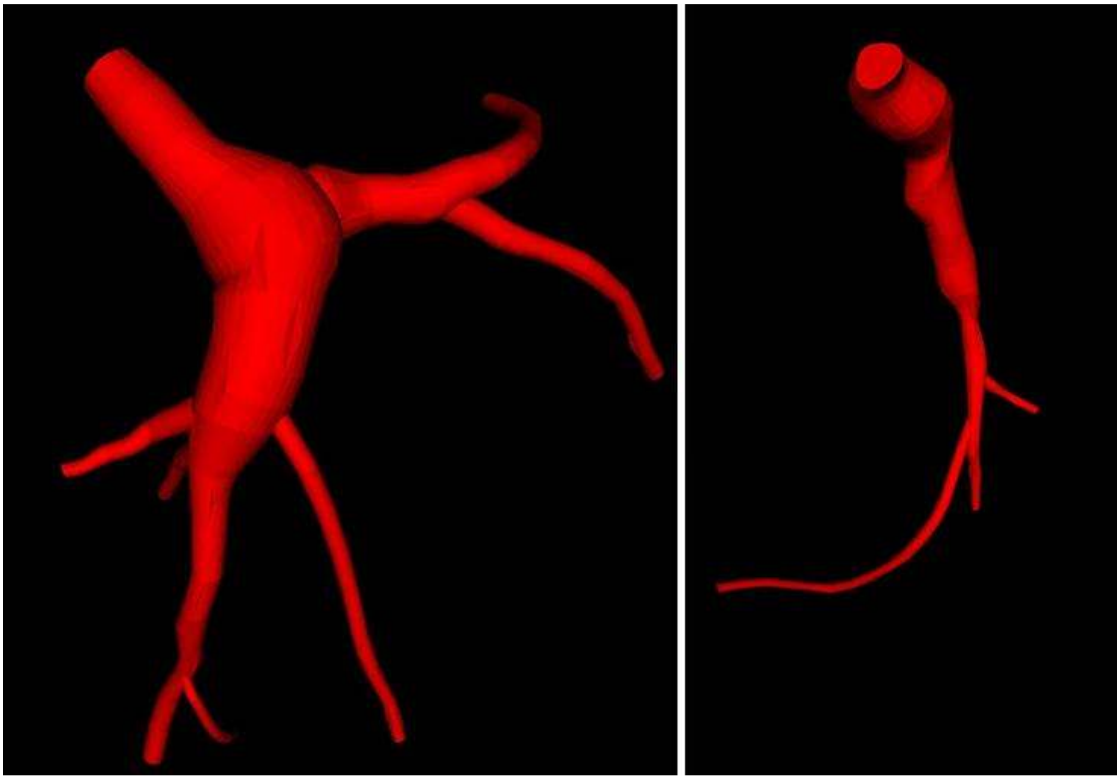

Figure 3.2: Reconstructed models of RCA (left) and RCA (right).

The input used for simulation consists of a typical coronary input waveform, shown on Figure 1.2. The outflow boundary condition uses the resistance in the outlet tubing.

3.2. Block Phantom Construction

This section describes the steps taken from printed plastic negative to silicone block positive, taking similar steps as described in (Palafox, Wicker, & Elkins, 2003). A more detailed description is in Appendix A 1. The equipments used in this process are listed in Appendix A 7.

To start the hardware construction, we imported the data into stereo lithography files (.STL) using SolidWorks CAD software.

Figure 3.3: CAD model of simplified RCA

This file was sent for 3D rapid-prototyping on a Dimension SSL 1200es machine to be printed with ABS plastic using FDM (Fused Deposition Modeling) process. The printed product is shown in Figure 3.4. The following steps were used for phantom construction:

Figure 3.4: Plastic negative printed from rapid-prototyping machine

1. Coat plastic negative with primer (Figure 3.5); this smoothes any roughness on the model

2. Cast printed model in two-part polyurethane resin (Figure 3.6)
3. Make wax negative from resin cast positive (Figure 3.7). Use microcrystalline wax that solidified with smooth surface (compared to paraffin wax)
4. Primer-coat, glue-coat wax negative (Figure 3.8). The glue coating will insulate the primer from silicone to preserve clarity in the final product

Figure 3.5: Primer-coated plastic model

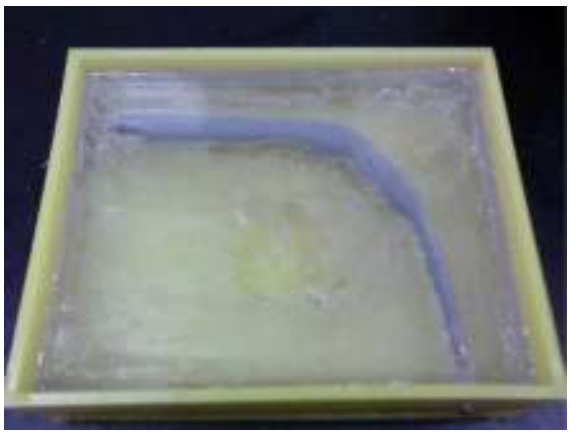

Figure 3.6: Plastic negative casted in polyurethane resin

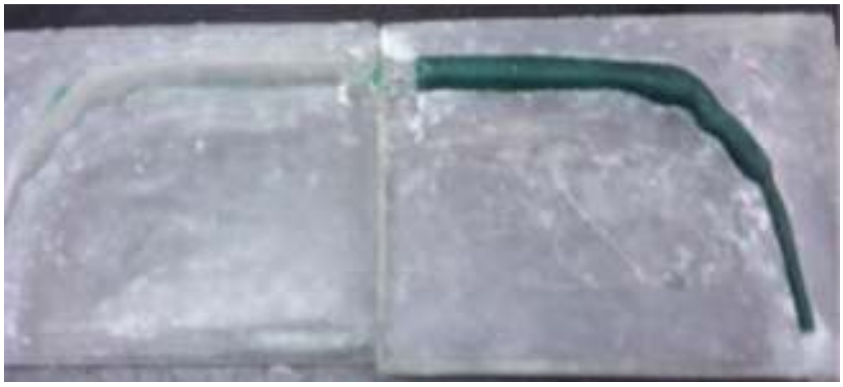

Figure 3.7: Wax negative made from resin positive

Figure 3.8: Primer-coated and glue-coated wax negative

5. Cast wax model in silicone (Figure 3.9)

Figure 3.9: Wax negative casted in silicone

6. Melt out wax from silicone block (Figure 3.10)

Figure 3.10: KD silicone block phantom

There are some limitations to this methodology. Though primer and glue coating helps smooth the product, the radius of the wax model shown in Figure 3.8 is increased. The final product will have a flow passage that's larger than the 3-D model that was printed, Figure 3.4. In future works, this could be compensated by measuring thickness of coating through each step to ensure the dimension accuracy.

Chapter 4. PIV Procedure

The working fluid must have properties that: 1. Match the index of refraction of the silicone, 2. Match the kinematic viscosity dynamic similarity. (Palafox, Wicker, & Elkins, 2003) A Glycol-water mixture was used for its blood-mimicking viscosity. Lycopodium powder was used as the fluorescent particle for visualization; it was mixed into the working fluid before filling the pump.

The pulsatile flow waveform shown in Figure 4.1 was used; data points for this profile are attached in Appendix A 2.

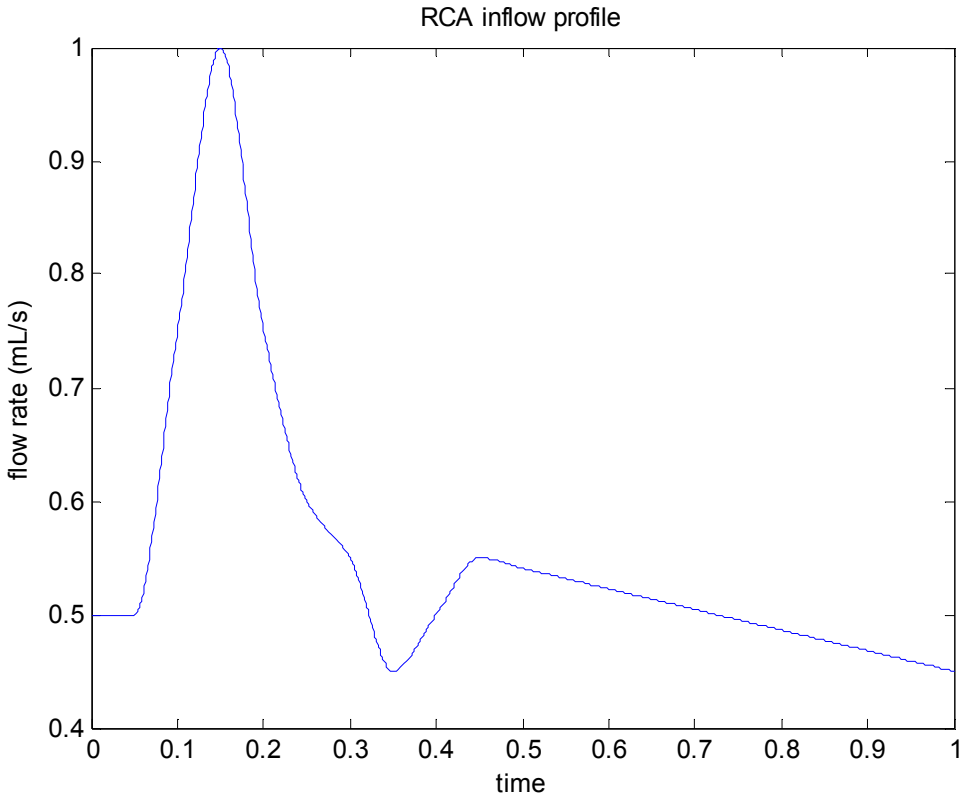

Figure 4.1: Input flow rate profile for RCA

Chapter 5. Results & Discussion

PIV data was taken at 14.5-Hz and processed in Insight 3G software. Holes in the data were interpolated and smoothed with low-pass filtering and the processed data is visualized with TecPlot.

Simulation data uses Figure 4.1 as the input and resistance from tubing as the outlet to match the in-vitro setup. The flow solver used for simulation is a custom finite element solver that solves 3-D, unsteady Navier-Stokes equation with second order accuracy. There are approximately 211,000 elements in the model mesh, with the mesh size chosen according to Courant-Friedrichs-Lewy condition.

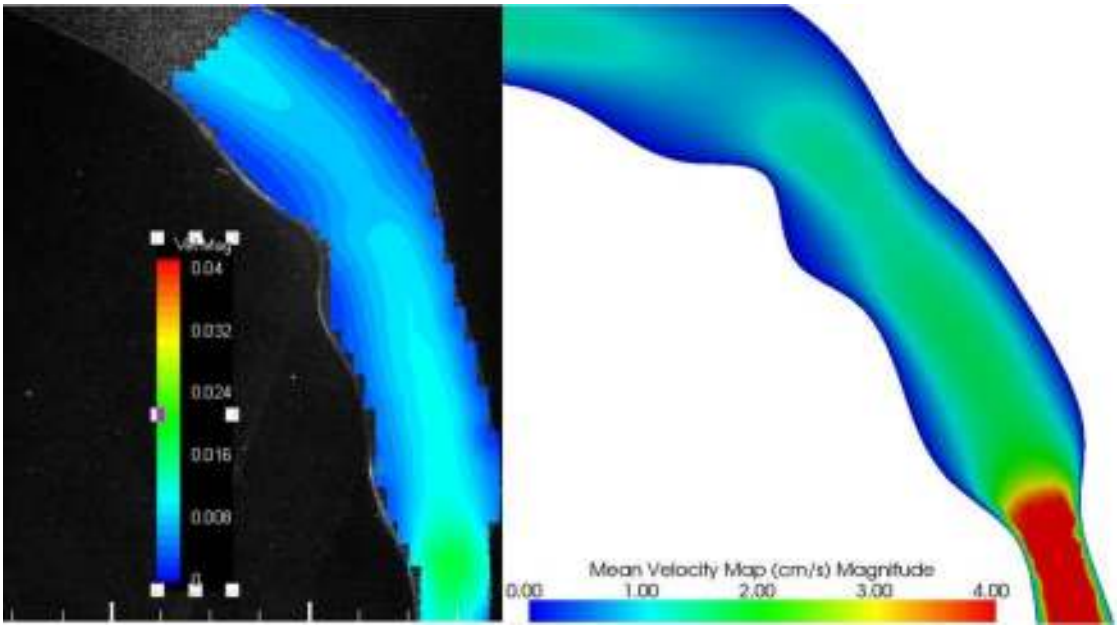

Figure 5.1: Time-averaged velocity contour of PIV (left) and simulation (right) data

Figure 5.1 shows the comparison between PIV and simulation data, based on time averaged velocity over one cycle of input, assuming cycles produce identical velocity profiles. Simulation data displays similar features throughout the contour,

including greatest magnitude of velocity at the stenosis and slower flow along the walls of the bulging sections. With both contours on the same scale, PIV data displays lower velocity magnitude throughout the contour. This may be due to error in the model construction process or the data taking process, which will later be discussed in section 5.1.

In a close-up view shown in Figure 5.2 at the bulging sidewalls, the instantaneous streamlines display the recirculation regions along areas of lower velocity magnitude. The specific point in the input cycle can be found on in Appendix A 3.

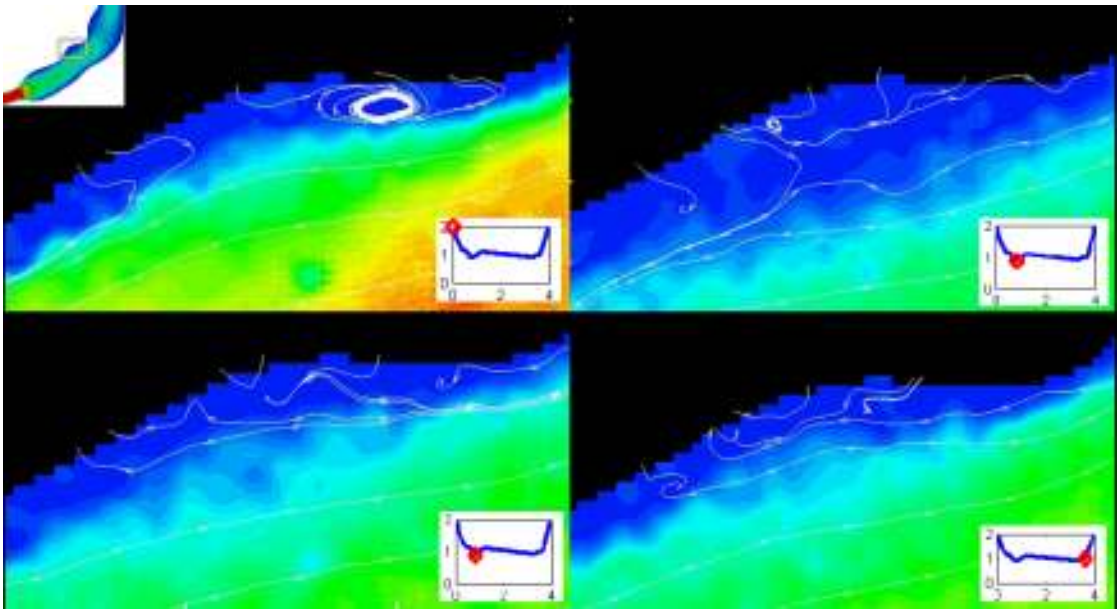

Figure 5.2: PIV streamline snap-shots at different points of the input cycle

For quantitative comparison, the difference between velocity profiles is examined. Overlapping the PIV and simulation results on the same plot, all of the profile pairs display the same skewing direction at their respective locations, shown in Figure 5.4, Figure 5.5, and Figure 5.6 with the locations referenced on Figure 5.3.

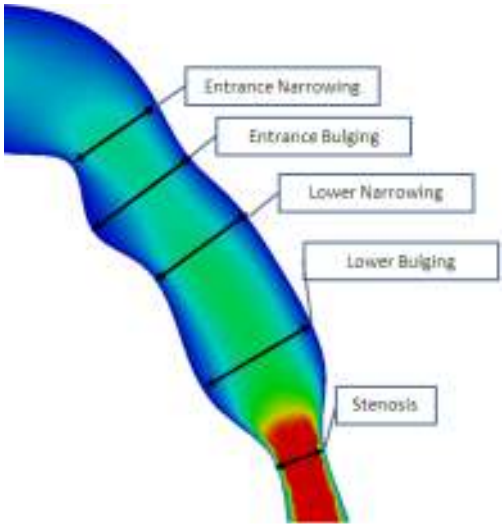

Figure 5.3 : Reference diagram for velocity profile sections

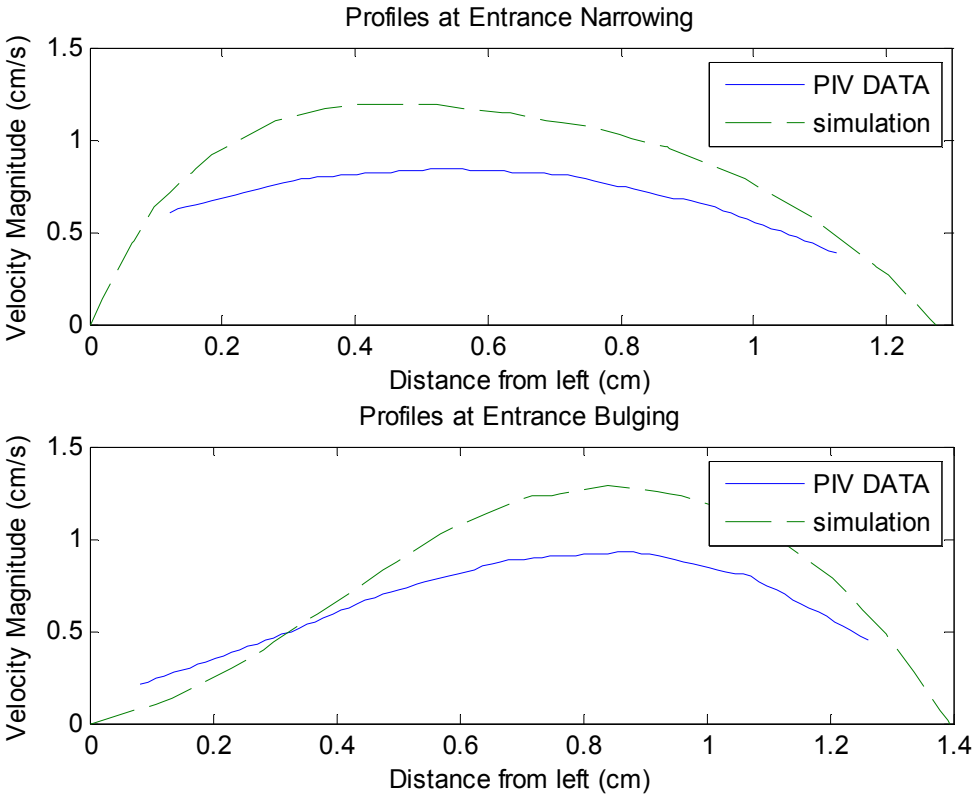

Figure 5.4: Time-averaged velocity profile at entrance cross sections

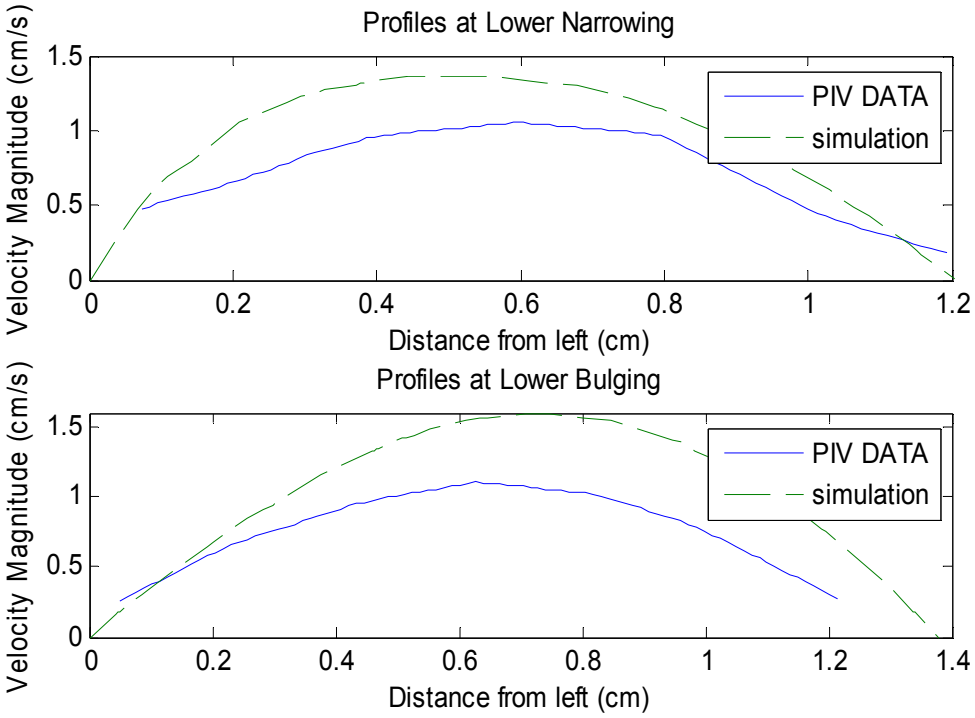

Figure 5.5: Time-averaged velocity profile at lower cross sections

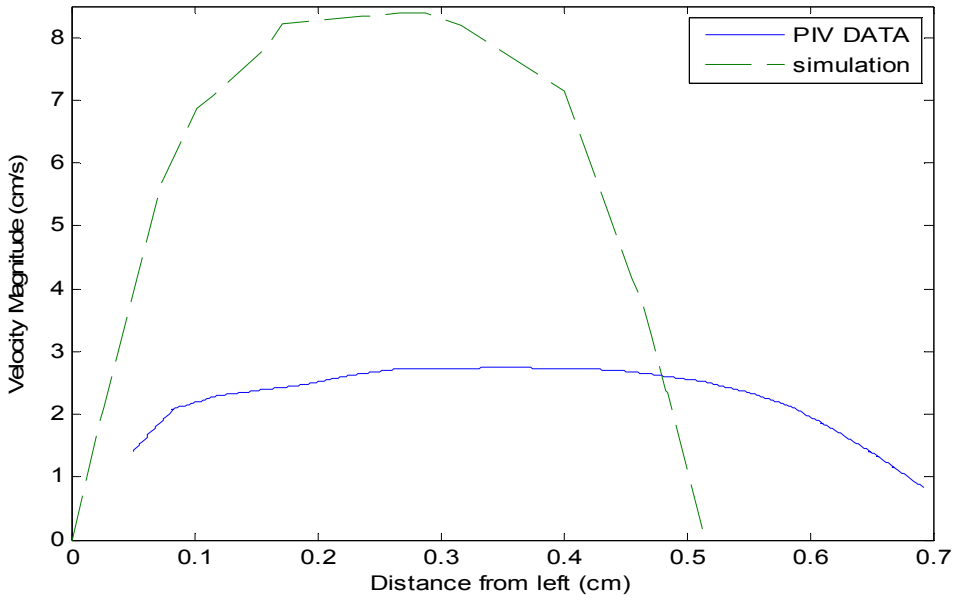

Figure 5.6: Time-averaged velocity profile at stenosis

Due to the lack of data at flow boundaries and the similar parabolic flow throughout PIV data, the peak velocity magnitudes are used to enumerate the difference; the results are summarized in Table 5.1. A consistently lower velocity magnitude is observed in the PIV data.

Table 5.1: Summary of Difference in Peak Velocity data (time-averaged)

	Entrance Narrowing	Entrance Bulging	Lower Narrowing	Lower Bulging	Stenosis	Averaged
% Error	29.35%	27.82%	23.02%	30.94%	27.78%	37.88%

5.1. Quantification for error

The PIV data consistently exhibit a lower velocity magnitude when compared to the simulation. Retracing the steps through the data taking process, we found that the laser may have been projected on a slanted plane, instead of the ideal center plane of the phantom. To verify that this was a cause of error, a slanted cross section was taken from the simulation data for the same quantitative comparison. The velocity profile at stenosis is shown in Figure 5.7 to compare the difference in magnitude. Velocity profiles at the other cross sections are shown in Appendix A 4.

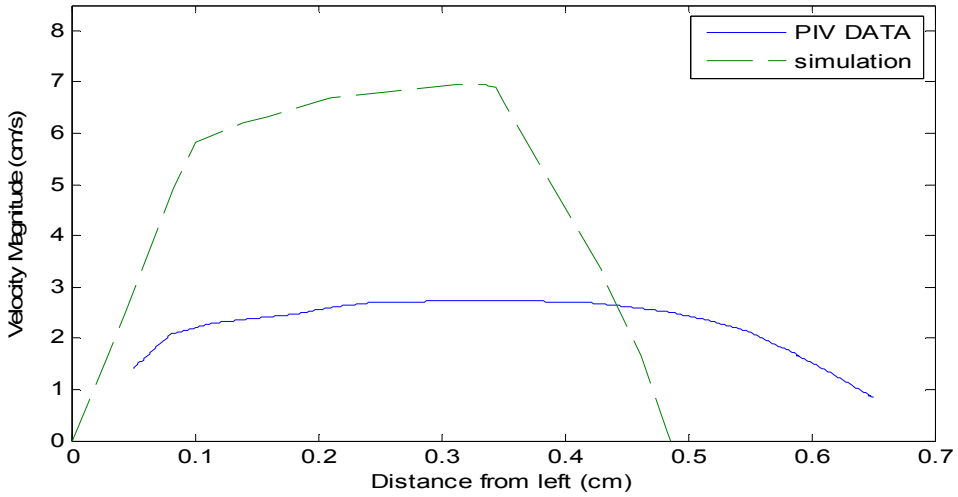

Figure 5.7: Time-averaged velocity profile at stenosis for a slanted cross section

As we can observe from both Figure 5.6 and Figure 5.7, the PIV data is displaying a longer width than that of the simulation data. This discrepancy can be traced to the limitations in the model construction, in which the negative model was thickened with layers of primer and glue coating. To numerically calculate this impact, another computational simulation was performed with a modified stenosis width matching that of the silicone model. The comparison is summarized in Table 5.2. The two velocity profiles from simulation are compared in Figure 5.8, showing a reduction of the peak velocity from 8.40 cm/s to 2.64 cm/s. This is reasonable because for two models with the same input flow rate, the model with a larger cross section (the phantom model) is expected to have a smaller velocity magnitude.

The modified stenosis profile is shown in Figure 5.9 with the other cross sections in Appendix A 5. We can observe that the magnitude more closely matches than those listed in the previous section.

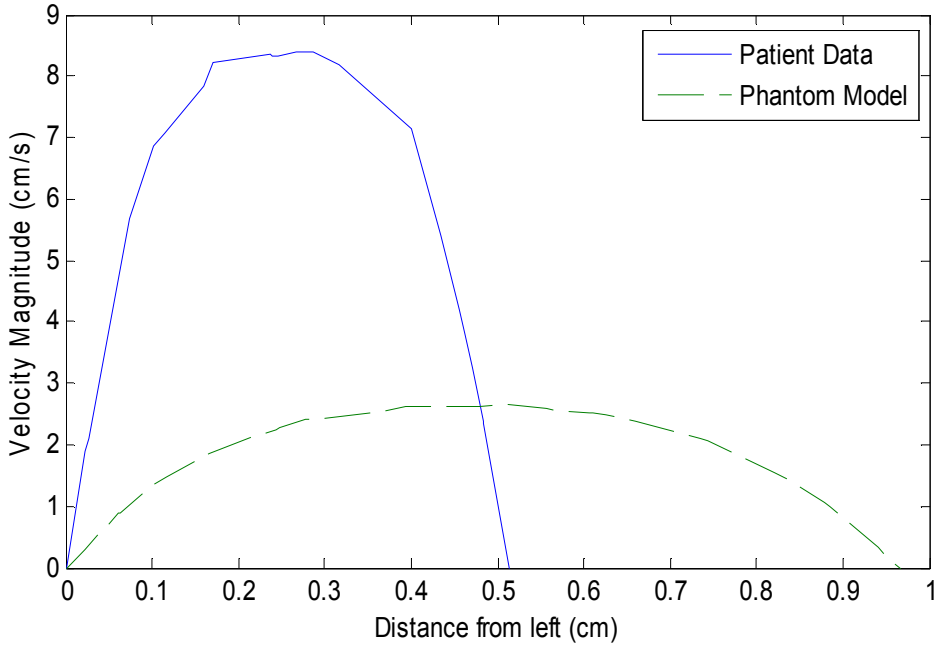

Figure 5.8: Time-averaged velocity profiles at stenosis from 2 different computational simulations

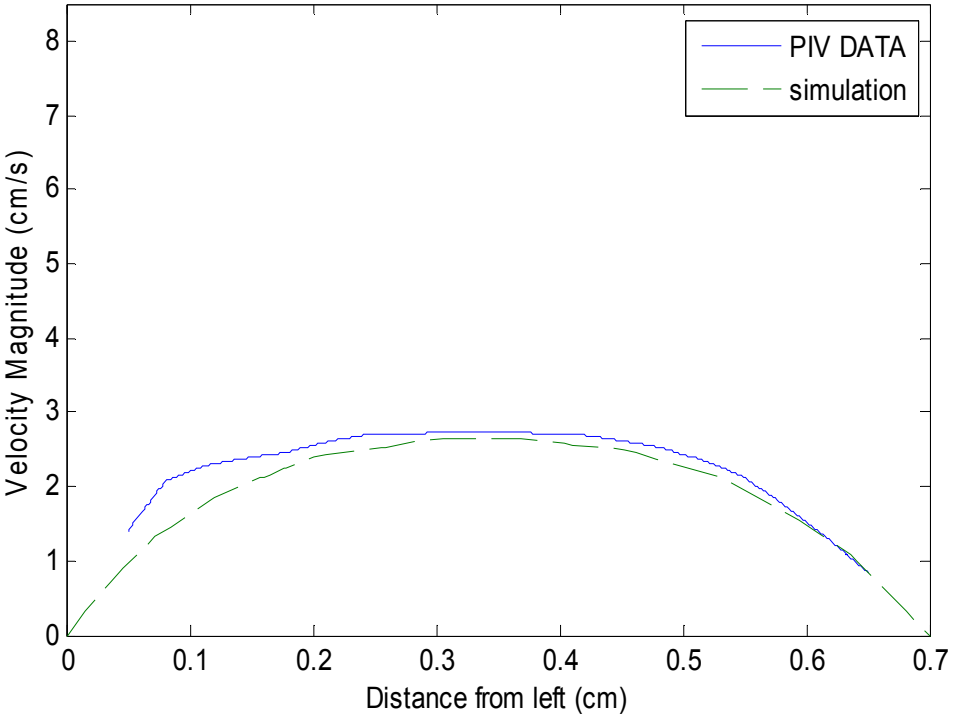

Figure 5.9: Time-averaged velocity profile at stenosis for model with phantom width

Considering that both of the mentioned errors are present, another profile comparison is shown in Figure 5.10 and Appendix A 6. The PIV profile has a slightly higher magnitude.

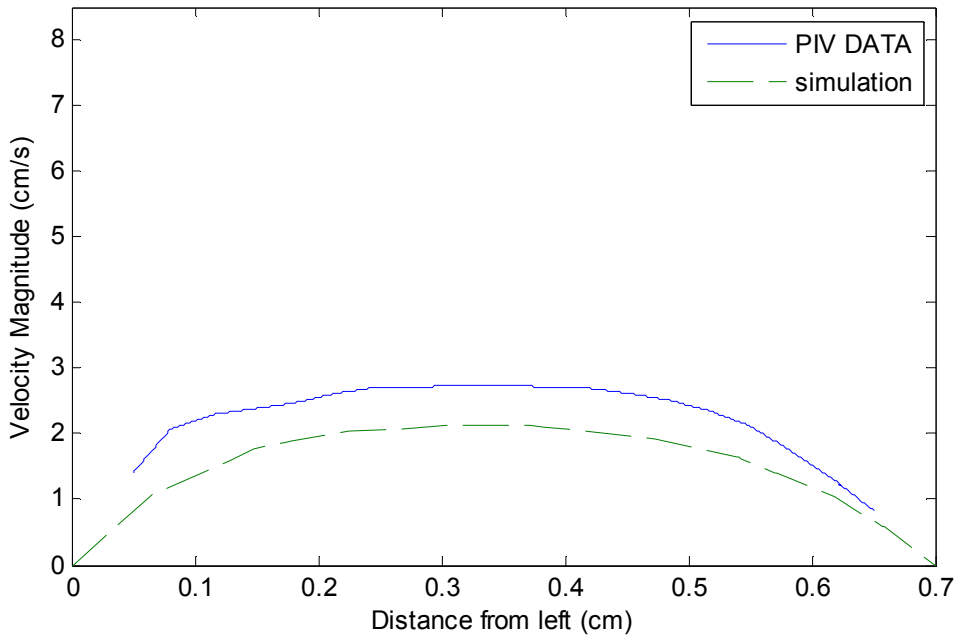

Figure 5.10: Time-averaged velocity profile at stenosis with phantom width at slanted cross section

Based on the numerical comparison, the enlarged diameter model, summarized as Case 3 in Table 5.2, had the greatest impact on the error since it lowered the error by more than half, especially in the stenosis region from 67% to 4%. The slanted view, Case 2, could also have contributed to the error, but not nearly as significant as the enlarged diameter issue. When incorporating both of the possible factors, shown as Case 4, the simulation scenario still displays a slightly higher percentage in error. These error percentages point to enlarged stenosis section as the main source of error.

Table 5.2 : Quantitative comparison of hypothsized error

Cases	Entrance Narrowing	Entrance Bulging	Lower Narrowing	Lower Bulging	Stenosis	Averaged
1. Ideal	29.35%	27.82%	23.02%	30.94%	67.43%	35.71%
2. Slanted	33.53%	30.57%	24.26%	26.49%	60.72%	35.11%
3. Phantom width	26.32%	26.10%	15.57%	15.29%	3.57%	15.94%
4. Both	26.07%	31.89%	29.83%	28.64%	28.06%	17.68%

5.2. Checking for time-dependence in the PIV data

The results shown in Chapter 5 above are computed over one input cycle. To investigate whether these results vary in time, the profiles of three consecutive cycles were plotted with error bars of one standard deviation in Figure 5.11, Figure 5.12, Figure 5.13, and Figure 5.14.

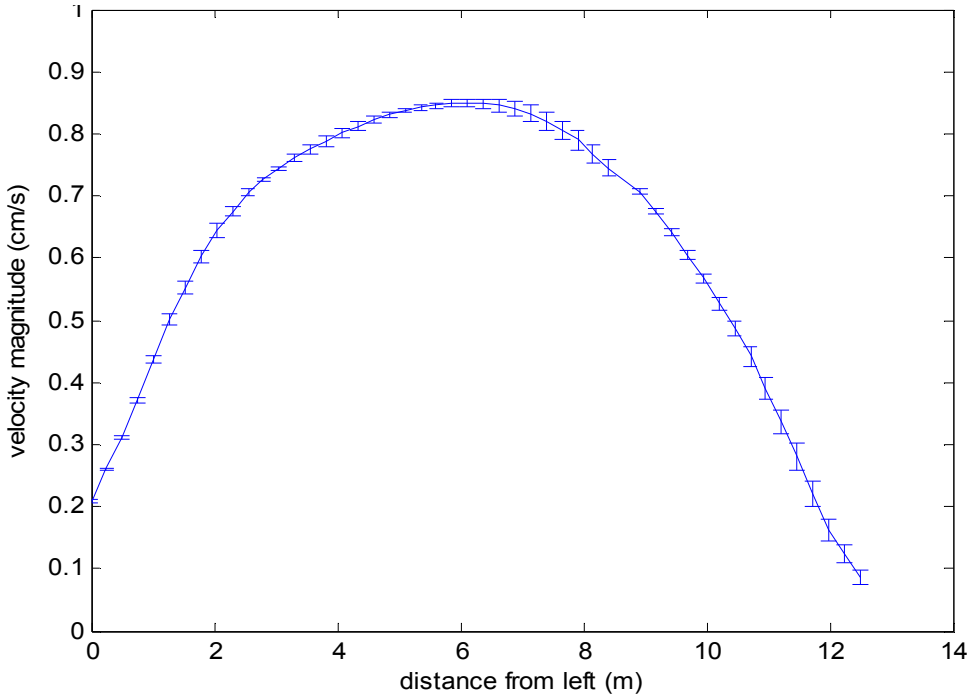

Figure 5.11: Time-averaged velocity profile over 3 input cycles at entrance narrow section

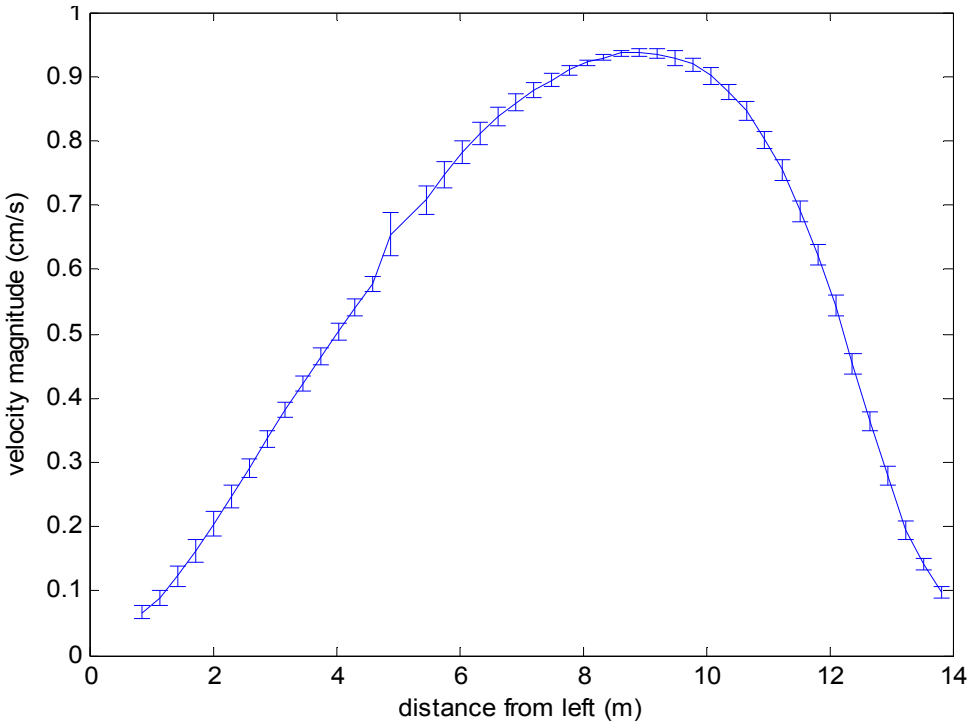

Figure 5.12: Time-averaged velocity profile over 3 input cycles at entrance bulk section

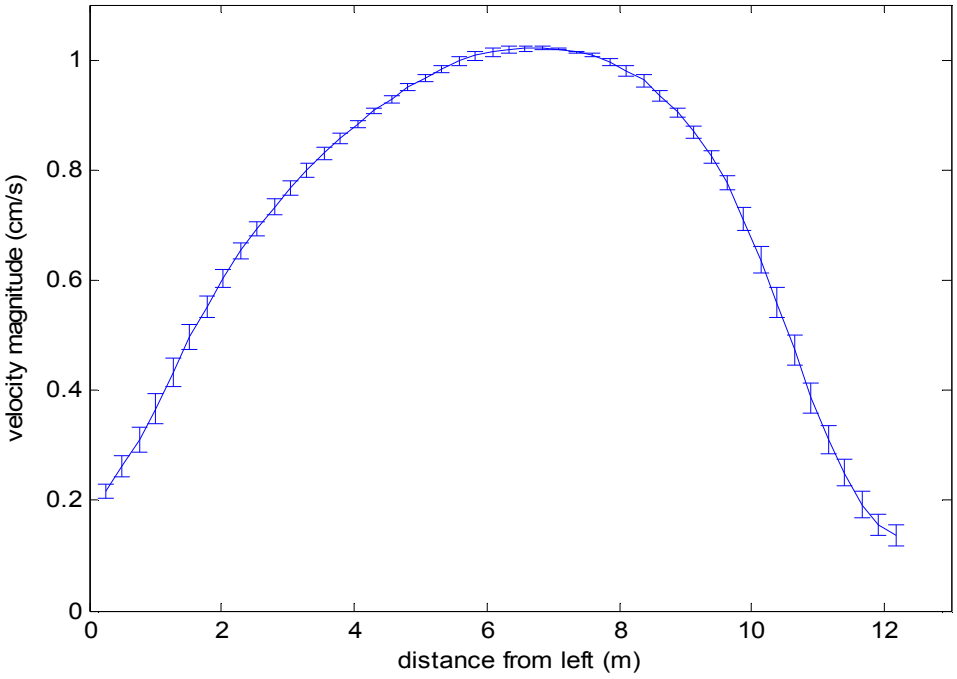

Figure 5.13: Time-averaged profile over 3 input cycles at lower narrow section

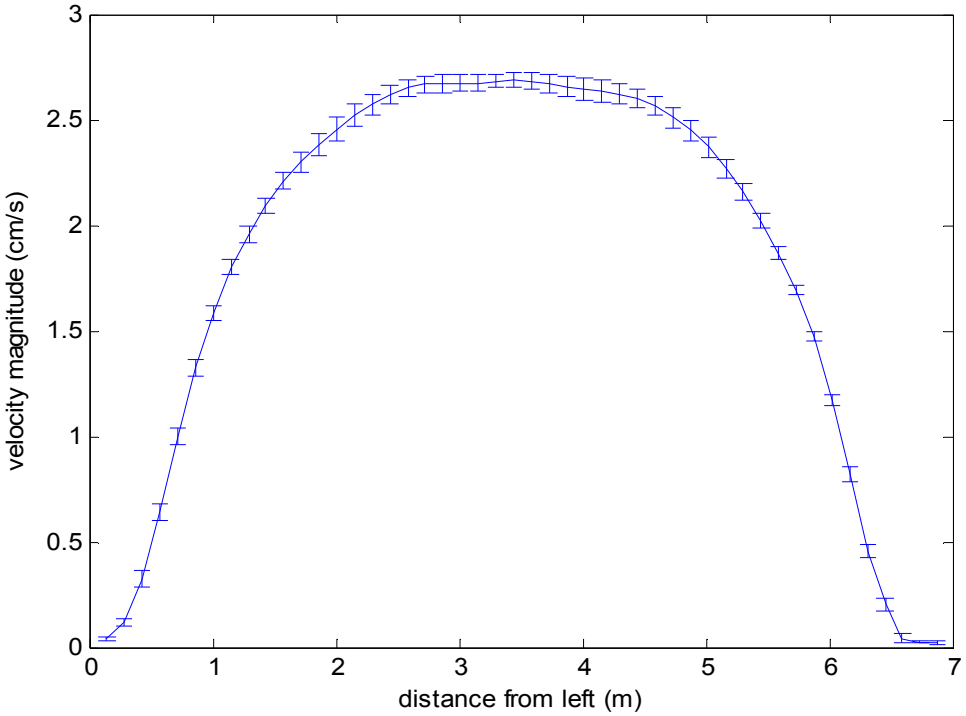

Figure 5.14: Time-averaged velocity profile over 3 input cycles at stenosis

The four sampled locations have a maximum standard deviation of 0.0211 cm/s, 0.0334 cm/s, 0.0284 cm/s, and 0.554 cm/s respectively in Figure 5.11, Figure 5.12, Figure 5.13, and Figure 5.14. The small magnitude in standard deviation demonstrates that the PIV data and results have no significant variation in time between the different cycles, and thus the flow profiles are indeed periodic and independent of time.

Chapter 6. Limitation of methodology

There were many imperfections from the experimental setup to acquire data. Starting from the phantom construction, the numerous handling processes created imperfections along the model surface. These imperfections may have been unintentionally preserved and were translated into roughness in the silicone phantom. This roughness may change some of the original flow features.

In the hardware setup, the pressure gradient and output flow rate of UHDC pump were calibrated in an open-loop setting. However, the data measurements were performed using UHDC in a closed loop setting where the output of the pump was connected to the input of the pump. The closed loop setting was not calibrated; therefore, there might be potential discrepancy caused by a reduction of input flow from the pump.

The experimental inflow was assumed to have a parabolic profile because it is simpler to simulate. However, the coronary artery is connected to the aorta in a curved instead of straight path, as shown in Figure 1.1, thus the flow from the aorta to the RCA may not be parabolic.

During the PIV data measurement process, we observed refraction of laser at fluid-phantom contact surface, affecting the accuracy of the data. When looking closely at the raw data, we can also notice some micro-particles sticking to the phantom surface, even at locations with high flow rate. This impacted the data processing filters to ignore the surface boundary and thus creating the lack of boundary data as shown in Figure 5.1 and Figure 5.2.

Chapter 7. Future Directions

With the constructed phantom, finer-resolution data should be taken. For a more comprehensive set of data, other cross sections of the phantom should be explored, eventually constructing a set of 3-D PIV data. Another important flow feature, the particle residence time in KD model, should also be measured.

In model construction, the mentioned dip-spin method can create an accurate phantom. Since the inaccuracy in the geometry was the largest contributing factor to the results in this thesis, the elimination of this problem will be necessary to proceed.

In order to fully validate the computational simulation tool, physiological conditions should be replicated in-vitro. For truly physiological flow, volumetric flow rate, pressure, and geometry should all be matched, just as used in computational simulations (Yang, Feinstein, & Marsden, 2010). The pressure was uncontrolled in this experiment; applying pressure gradient across inlet-outlet could potentially change the results. The input waveform was also simplified with an assumption that it has a parabolic profile; finding the exact profile shape for input into the coronary artery currently remains a challenge.

In performing the computational simulations of KD model, some of the challenges include the pressure that is not in sync with the flow rate. This was observed from the peak flow rate and the maximum pressure occurring at different moments of a cycle. In order to more accurately replicate coronary flow, the simulation would first need to be improved to meet the out-of-sync conditions.

Chapter 8. Conclusion

This project has put together a setup for in-vitro validation experimentation. From replicating the inflow condition to constructing an anatomically correct flow phantom, we have created a similar flow profile in KD aneurysm that can be studied with PIV measurements. The data acquired from this setup can be used for direct comparison with the data from computational simulations.

As compared in Figure 5.1, the major flow features from PIV match that of the simulation. These features include recirculation areas and skewed parabolic velocity profile. The prevailing difference is the reduced velocity magnitude shown throughout the PIV data.

Though there are still discrepancies between the two sets of data as shown in Chapter 0, this thesis has shown that the methodology is feasible. This lays the groundwork for in-vitro validation using patient specific data. Anatomy of different shapes and sizes can also use the process described in this thesis to build another flow phantom and perform validation.

Appendix

A 1. Block Process Details

1. Post-processing plastic model
    a. Drill tap both ends of plastic model
    b. Spray coat plastic model with primer paint

    c. Sand model surface until smooth
    d. Coat with mold release. Model shown in Figure 3.5
2. Casting in resin
    a. Condition acrylic box concave with mold release
    b. Suspend plastic model in acrylic box[1]

[1] Suspend model by fixing BOTH ends onto the wall. Free end may pop out of resin when curing

c. Mix resin and catalyst per prescribed on product
d. Fill resin up to widest cross section of plastic model [2] ; give at least two days of curing time

e. Condition surface again with mold release solution
f. Fill box with resin to complete second half of resin mold, shown in Figure 3.6.
g. Take resin mold out of acrylic box

h. Clean out plastic model to get two halves of the mold

[2] For model to release, connecting faces of mold must be the widest cross section of model,

3. Molding wax model (using microcrystalline wax[3])
    a. Clamp together resin mold
    b. Fill resin with melted wax
    c. Wait five minutes[4]; chill mold and wax in refrigerator for two hours. Completed wax model shown in Figure 3.7.
4. Coating silicone phantom
    a. Primer-coat wax model
    b. Glue-coat wax model
    c. Attach connectors to ends of wax model, shown in Figure 3.8
    d. Mount model in acrylic box and seal holes

    e. Mix silicone base with agent, de-air mixture using vacuum
    f. Fill box with de-aired silicone mix, shown in Figure 3.9. Give at least four days of curing time.

---

[3] Jeweler's wax used

[4]To avoid air bubbles at outer surface of wax model

5. Cleaning out the wax model
    a. Melt out wax model in 250°F oven
    b. Use acetone to wash out most of primer coating
    c. Pull off the glue coating for clear passage. Small residues can be cleaned by running de-ionized water through the passage.

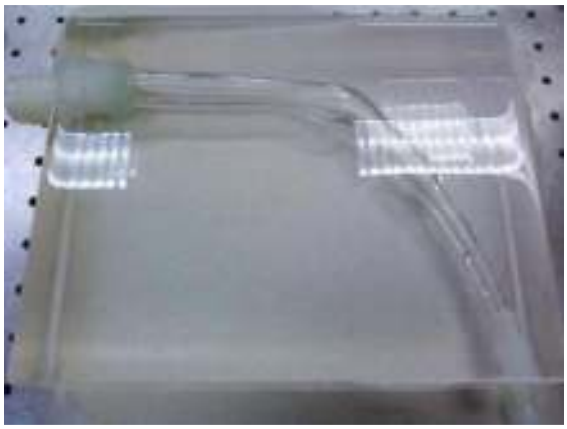

A 2. KD Inflow Data Points

KD_sample = [timestep flowrate]
KD_sample =

0	0.5000	0.3400	0.4593	0.6800	0.5082
0.0100	0.5000	0.3500	0.4500	0.6900	0.5064
0.0200	0.5000	0.3600	0.4532	0.7000	0.5046
0.0300	0.5000	0.3700	0.4621	0.7100	0.5028
0.0400	0.5000	0.3800	0.4744	0.7200	0.5010
0.0500	0.5000	0.3900	0.4876	0.7300	0.4991
0.0600	0.5149	0.4000	0.4994	0.7400	0.4973
0.0700	0.5589	0.4100	0.5108	0.7500	0.4955
0.0800	0.6199	0.4200	0.5240	0.7600	0.4937
0.0900	0.6861	0.4300	0.5366	0.7700	0.4919
0.1000	0.7454	0.4400	0.5460	0.7800	0.4900
0.1100	0.8023	0.4500	0.5500	0.7900	0.4882
0.1200	0.8682	0.4600	0.5494	0.8000	0.4864
0.1300	0.9311	0.4700	0.5478	0.8100	0.4846
0.1400	0.9790	0.4800	0.5455	0.8200	0.4828
0.1500	0.9999	0.4900	0.5431	0.8300	0.4809
0.1600	0.9830	0.5000	0.5410	0.8400	0.4791
0.1700	0.9349	0.5100	0.5392	0.8500	0.4773
0.1800	0.8705	0.5200	0.5374	0.8600	0.4755
0.1900	0.8049	0.5300	0.5355	0.8700	0.4737
0.2000	0.7531	0.5400	0.5337	0.8800	0.4718
0.2100	0.7157	0.5500	0.5319	0.8900	0.4700
0.2200	0.6801	0.5600	0.5301	0.9000	0.4682
0.2300	0.6479	0.5700	0.5283	0.9100	0.4664
0.2400	0.6210	0.5800	0.5264	0.9200	0.4646
0.2500	0.6012	0.5900	0.5246	0.9300	0.4627
0.2600	0.5881	0.6000	0.5228	0.9400	0.4609
0.2700	0.5786	0.6100	0.5210	0.9500	0.4591
0.2800	0.5706	0.6200	0.5192	0.9600	0.4573
0.2900	0.5620	0.6300	0.5173	0.9700	0.4555
0.3000	0.5509	0.6400	0.5155	0.9800	0.4536
0.3100	0.5327	0.6500	0.5137	0.9900	0.4518
0.3200	0.5070	0.6600	0.5119		
0.3300	0.4805	0.6700	0.5101		

A 3. Selected time points in inflow profile

This figure is the generated with data points on page 34. It shows the same waveform as shown in Figure 4.1 with a shift in time, such that the waveform starts with peak flow rate.

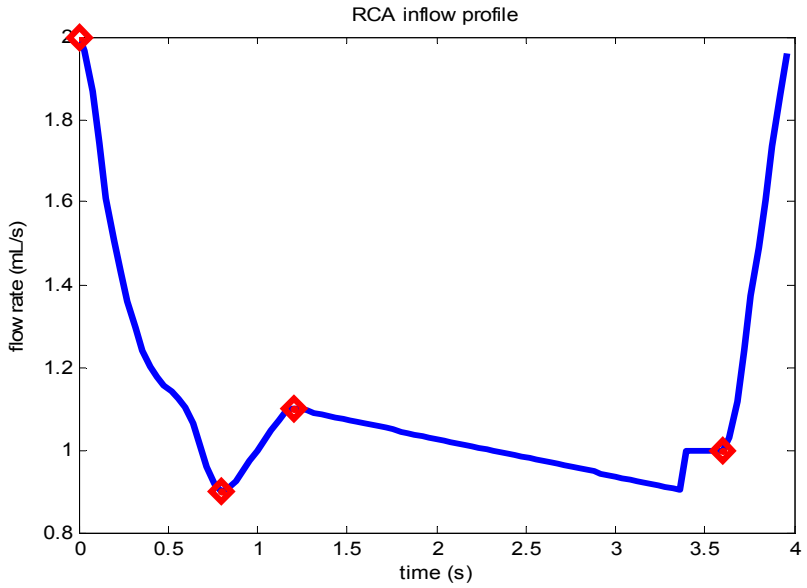

The points marked with red diamond shape are referenced as the ‘peak’, ‘valley’, ‘steady’, and ‘rise’, respectively from left to right.

A 4. Time Averaged Velocity Profiles at a slanted plane

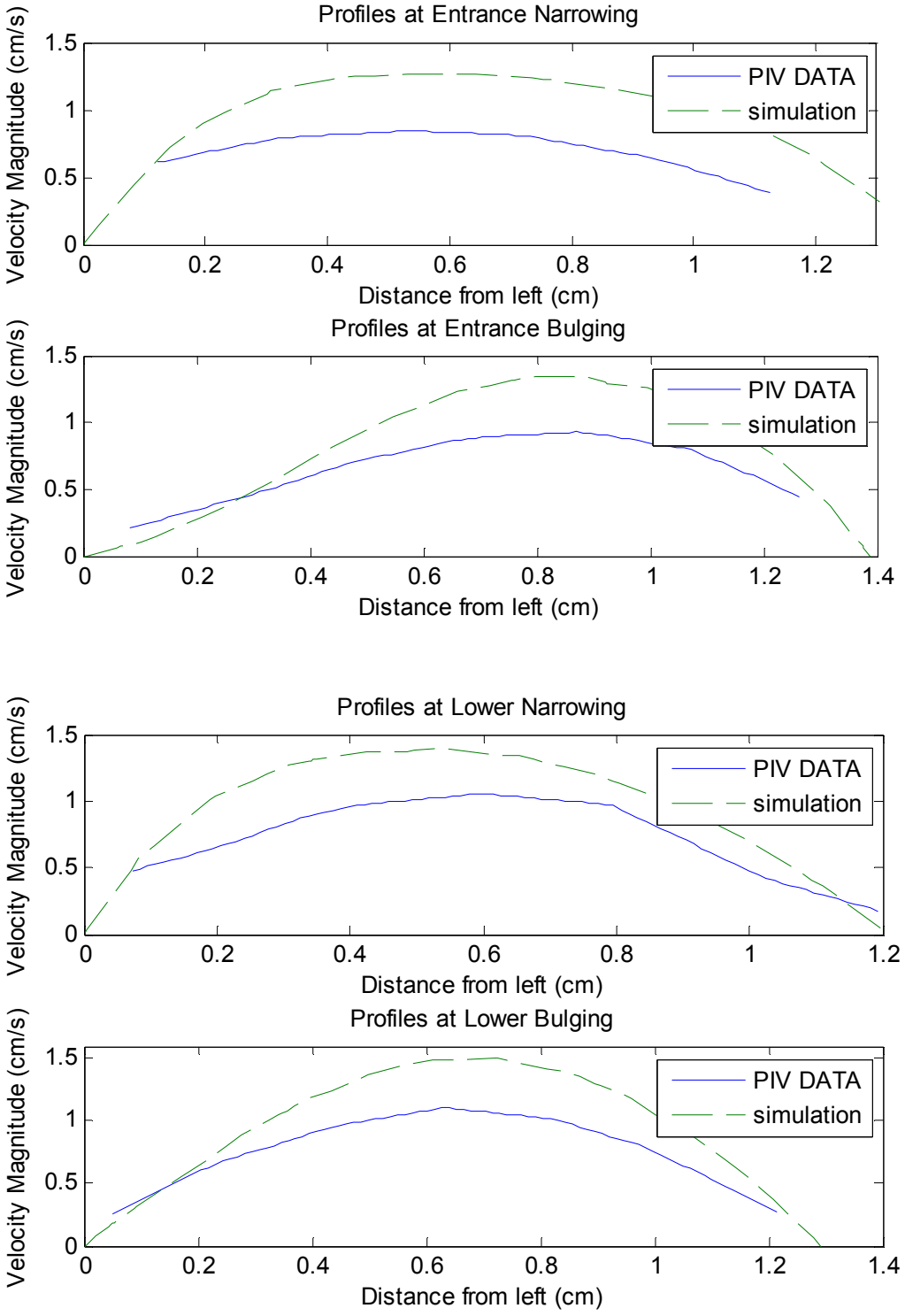

A 5. Time Averaged Velocity Profiles with phantom width

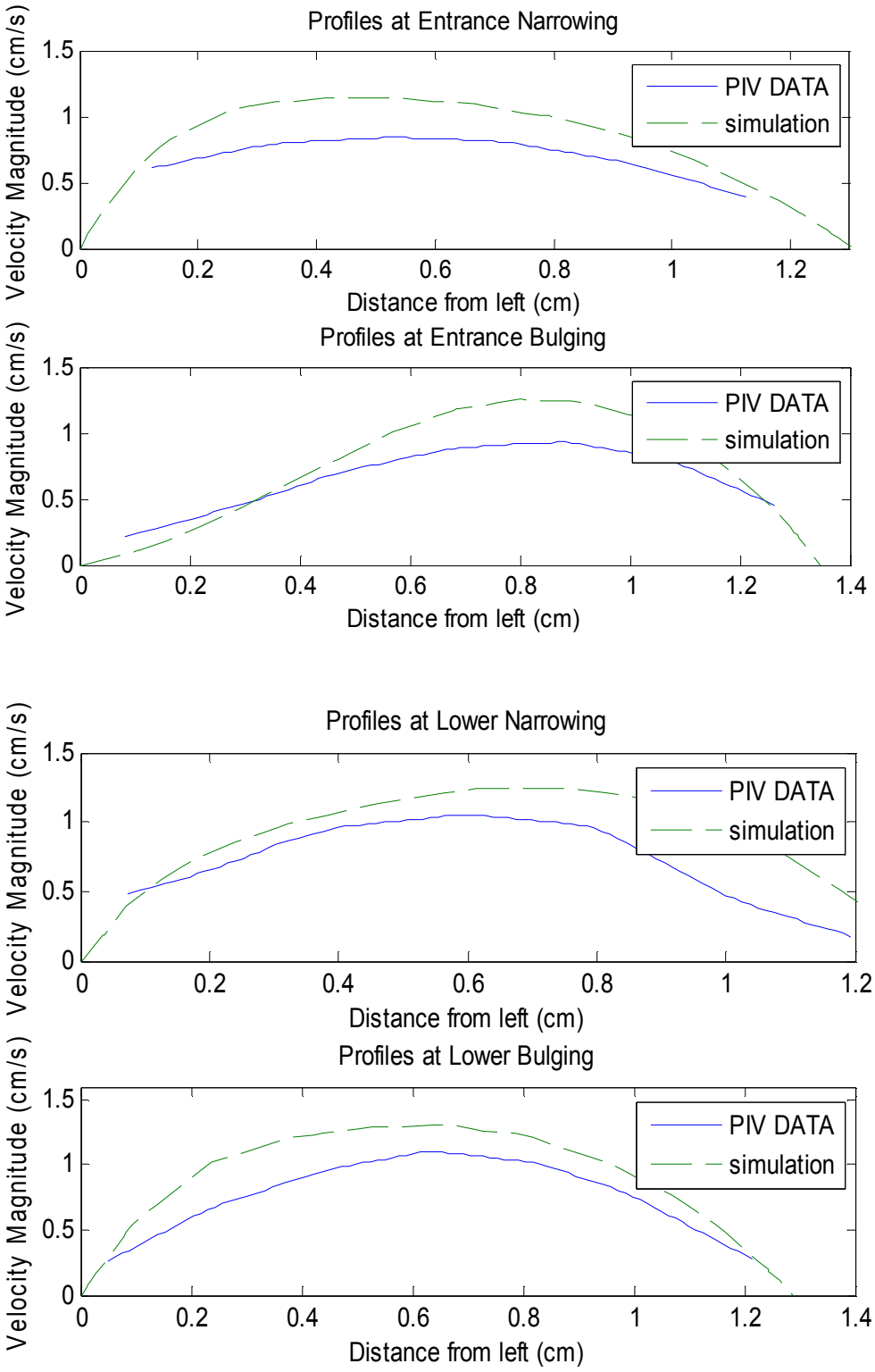

A 6. Time Averaged Velocity Profiles at a slanted plane & phantom width

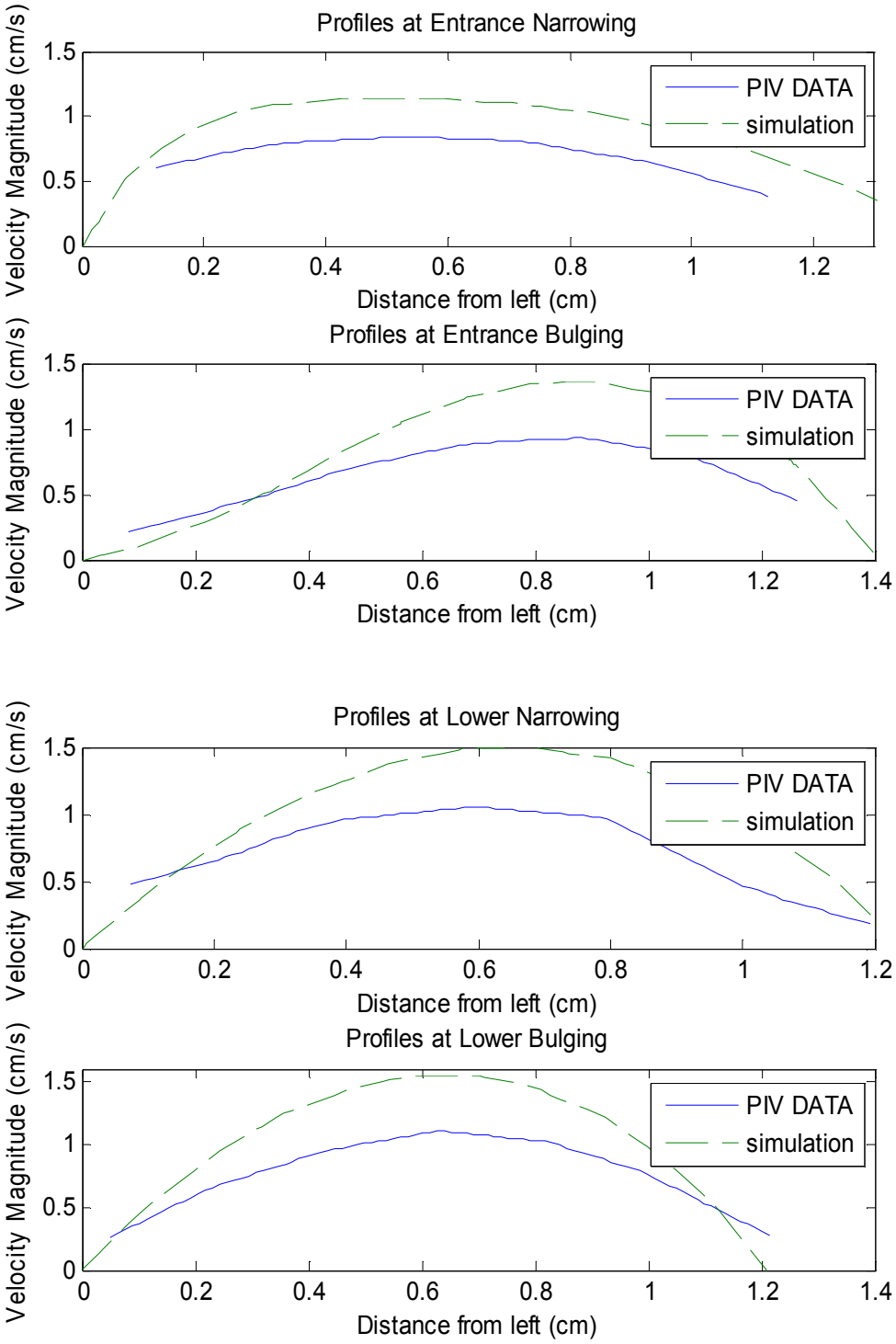

A 7. Equipment Listing

1. UHDC Flow System (Shelley Medical, London, Ontario, Canada)

2. PIV System

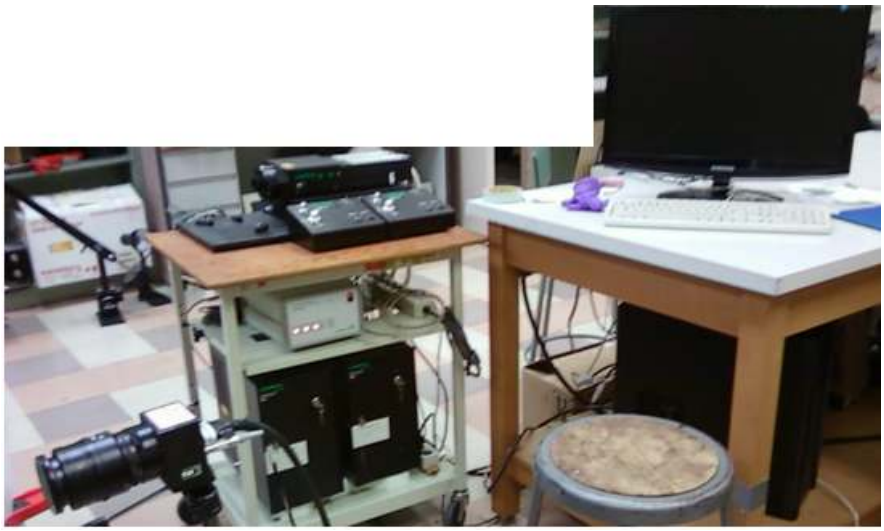

a. Lycopodium powder

3. Block Model Construction
    1) 3D Model Printed via Dimension SST 1200es
        a. Using Stratasys FDM (Fused Deposition Modeling) process, builds functional 3D models from the bottom up, one layer at a time with acrylonitrile butadiene styrene (ABS) plastic
    2) ¼-inch thick sheet Acrylic
    3) Acrylic Glue (Weld-On 3 Acrylic Adhesive)
    4) Silicone Sealant (Momentive RTV108 Electro Insulation - Clear)
    5) Mold Release & Conditioner
    6) Casting Resin
    7) Casting Resin Catalyst
    8) Jeweler's wax - Wire Wax assortment
    9) Elmer's glue – Washable
    10) SYLGARD® 184 SILICONE ELASTOMER KIT

Bibliography

Burns, J. C., & Glode, M. P. (2004). Kawasaki Syndrome. *Lancet* , 533-544.

Burns, J. C., Shike, H., Gordon, J. B., Malhotra, A., Schoenwetter, M., & Kawasaki, T. (1996). Sequelae of Kawasaki Disease in Adolescents and Young Adults. *Journal of the American College of Cardiology , 28* (1), 253-257.

Canton, G., Levy, D. I., Lasheras, J. C., & Nelson, P. K. (2005). Flow changes caused by the sequential placement of stents across the neck of sidewall cerebral aneurysms. *Journal of Neurosurgery* , 891-902.

Cortez, M. A., Quintana, R., & Wicker, R. B. (2007). Multi-step dip-spin coating manufacturing system for silicone cardiovascular membrane fabrication with prescribed compliance. *International Journal of Advanced Manufacturing Technology* , 667-679.

Duong, T. T., Silverman, E. D., Bissessar, M. V., & Yeung, R. S. (2003). Superantigenic activity is responsible for induction of coronary arteritis in mice: an animal model of Kawasaki disease. *Japanese Society for Immunology , 15* (1), 79-89.

Hale, J. F., McDonald, D. A., & Womersley, J. R. (1955). Velocity profiles of oscillating arterial flow, with some calculations of viscous drag and the Reynolds number. *The Journal of Physiology* (128), 629.

Isaksen, J. G., Bazilevs, Y., Kvamsdal, T., Zhang, Y., Kaspersen, J. H., & Waterloo, K. (2008). Determination of Wall Tension in Cerebral Artery Aneurysms by Numerical Simulation. *Stroke* , 3172-3178.

Kawasaki, T. (1967). Acute febrile mucocutaneous syndrome with lymphoid involvement with specific desquamation of the fingers and toes in children [In Japanese]. *Arerugi* , 16:178.

LaDisa, J. F., Guler, I., Olson, L. E., Hettrick, D. A., Kersten, J. R., & Warltier, D. C. (2003). Three-Dimensional Computational Fluid Dynamics Modeling of Alterations in Coronary Wall Shear Stress PRoduced by Stent Implantation. *Annals of Biomedical Engineering* , 972-980.

Leuprecht, A., Perktold, K., Prosi, M., Berk, T., Wolfgang, T., & Schima, H. (2002). Numerical study of hemodynamics and wall mechanics in distal end-to-side anastomoses of bypass grafts. *Journal of Biomechanics , 35* (2), 225-236.

Marsden, A. L., Bernstein, A. J., Reddy, V. M., Shadden, S. C., Spilker, R. L., & Chan, F. P. (2009). Evaluation of a novel Y-shaped extracardiac Fontan baffle using computational fluid dyanmics. *The Journal of Thoracic and Cardiovascular Surgery* , 394-403.

Palafox, G. N., Wicker, R. B., & Elkins, C. J. (2003). Rapid In-vitro physiologic flow experimentation using rapid prototyping and particle image velocimetry. *Summer Bioengineering Conference*, (pp. 0419-0420). Key Biscayne, Florida.

Strony, J., Beaudoin, A., Brands, D., & Adelman, B. (1993). Analysis of shear stress and hemodynamic factors in a model of coronary artery stenosis and thrombosis. *Am J Physiol Heart Circ Physiol* , 1787-1796.

Suzuki, A., Miyagawa-Tomita, S., Komatsu, K., Nishikawa, T., Sakomura, Y., & Horie, T. (1986). Active remodeling of the coronary arterial lesions in the late phase of Kawasaki Disease: immunohistochemical study. *Circulation* (101), 2935-2941.

Tang, B. T., Cheng, C. P., Draney, M. T., Wilson, N. M., Tsao, P. S., & Herfkens, R. J. (2006). Abdominal aortic hemodynamics in young healthy adults at rest and during lower limb exercise: quantification using image-based computer modeling. *American Journal of Physiology - Heart and Circulatory Physiology* , 668-676.

Taylor, C. A., Hughes, T. J., & Zarins, C. K. (1998). Finite Element modeling of Three-Dimensional Pulsatile Flow in the Abdominal Aorta: Relevance to Atherosclerosis. *Annals of Biomedical Engineering* , 975-987.

Wilson, N., Arko, F. R., & Taylor, C. (2004). Patient-Specific Operative Planning for Aorto-Femoral Reconstruction Procedures. *Medical Image Computing and Computer-Assisted Intervention - MICCAI 2004. 7th International Conference Proceedings*, (pp. 422-429).

Yang, W., Feinstein, J. A., & Marsden, A. L. (2010). Constrained optimization of an idealized Y-shaped baffle for t Fontan surgery at rest and exercise. *Computer Methods in Applied Mechanics and Engineering , 199* (33-36), 2135-2149.